MER-B *Opportunity* MI Calibration Processing Revisions

Ken Herkenhoff, Ella Lee, Janet Richie, Bob Sucharski, and Annette Sunda

U. S. Geological Survey Astrogeology Science Center, August 2019

Introduction

Pre-flight calibration of the Mars Exploration Rover (MER) Microscopic Imager (MI) cameras has been documented previously [Herkenhoff *et al*., 2003; 2004], and updates based on early MER-B "*Opportunity"* mission results were described by Herkenhoff *et al*. [2008]. The purpose of this document is to describe improvements to Opportunity MI calibration using data acquired later in the mission, after the MI optics were contaminated during the 2007 global dust storm on Mars and camera temperature telemetry became unreliable. These improvements have been applied to all *Opportunity* MI data acquired after the 2007 dust storm, and revised data products delivered to the Planetary Data System for archival storage.

Dark Current

There are 3 sources of dark current (thermal noise) in the MI cameras: the reference pixel (bias) component, zero-exposure component, and active-area component [Herkenhoff *et al*., 2003]. Because the MI has no shutter and its dust cover is transparent, it was impossible to acquire useful zero-exposure or active-area dark current data on the surface of Mars because nighttime temperatures were so low that dark current was insignificant. Therefore, preflight calibration data [Herkenhoff *et al*., 2004] were used to model these components of dark current as a function of temperature and correct inflight MI data. The reference pixels, however, are not illuminated and were returned with many images during the landed mission. These data were used to update the reference pixel model [Herkenhoff *et al*., 2008] that has been used to subtract this offset from each line of all MI images that were returned without reference pixels.

Each MI camera includes two temperature sensors, one near the charge coupled device (CCD) detector and another on the printed circuit board (PCB) in the electronics box. The camera head and electronics are separate assemblies connected by a flex cable (Herkenhoff *et al*., 2003), so that the two sensors are effectively thermally isolated from each other. About halfway through the *Opportunity* mission, MI CCD temperature data became unreliable. As shown in Figure 1, CCD temperatures varied seasonally, as expected, during the first 3 Mars years of the mission. During the first 2611 sols of the *Opportunity* mission, the MI CCD temperature never exceeded 21°C, so we assume that temperatures returned from the CCD temperature sensor that exceed that value are erroneous. Starting on Sol 2669, CCD temperature data were often null (0°C in Fig. 1), indicating intermittent failure of the temperature sensor.

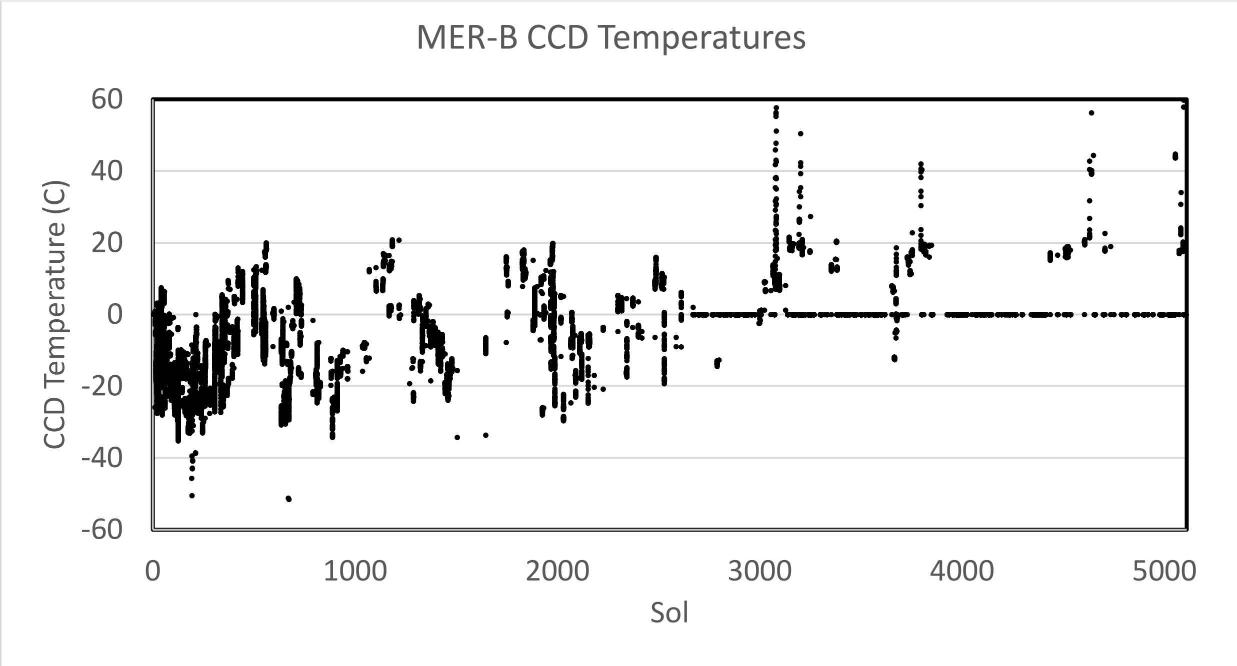

Figure 1. *Opportunity* MI CCD temperature in degrees Celsius vs. Sol number for the entire mission.

However, anomalous data are not seen in the *Opportunity* MI PCB temperatures (Fig. 2). Before the CCD temperature sensor failure, the difference between the CCD and PCB temperatures was always between -11.9 and 24.4°C (Fig. 3).

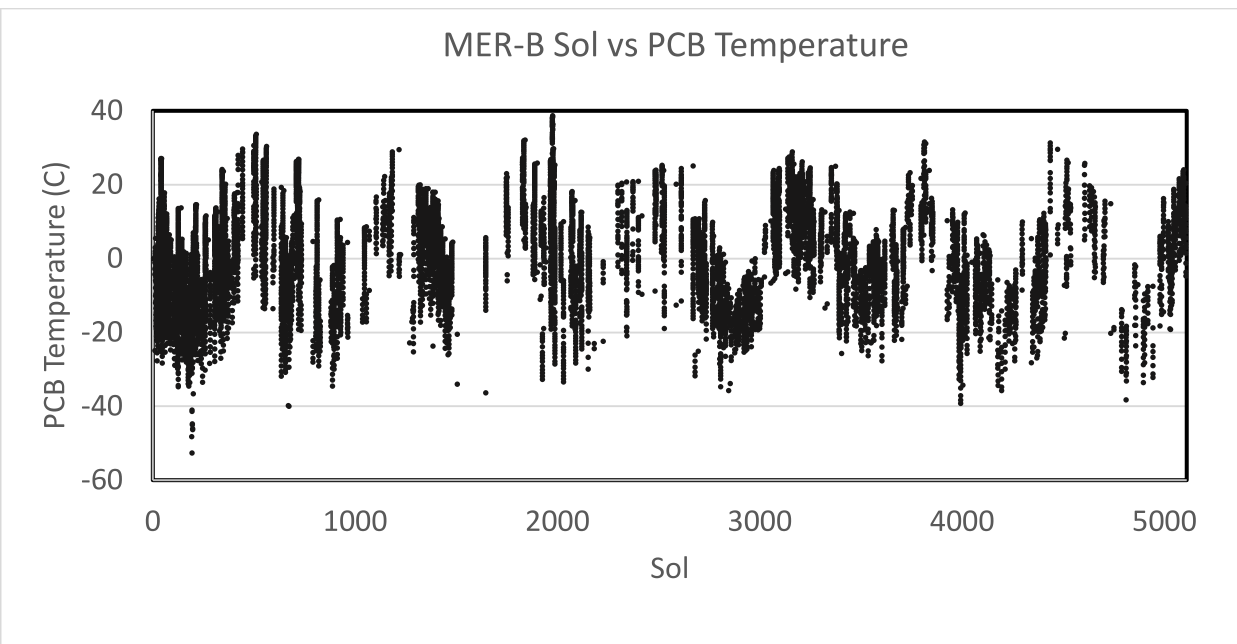

Figure 1. *Opportunity* MI PCB temperatures in degrees Celsius vs. Sol number for the entire mission.

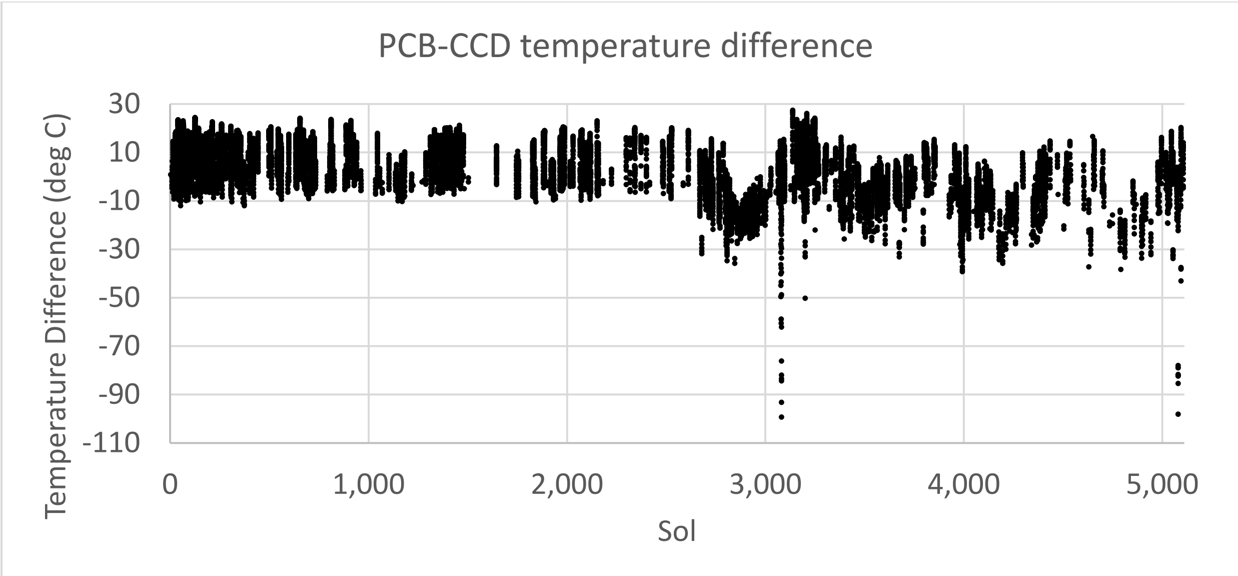

Figure 2. Difference between *Opportunity* MI PCB and CCD temperatures vs. Sol number.

Based on these observations, we consider all CCD temperature data returned after Sol 2611 suspect. Erroneous CCD temperatures significantly affect the accuracy of the MI zero-exposure and active-area dark current models: At the highest recorded valid MI CCD temperature (21°C) and a 1-second exposure time (worst case), dark current is about 200 DN (10% of a well-exposed image), so accurate modeling is desired. Therefore, we analyzed the difference between the PCB and CCD temperatures for each MI image acquired through Sol 2611, assuming that the PCB temperatures are reliable. As shown in Figure 4, this difference (normalized to the initial temperature difference in each series of MI images) increases with time as the MI electronics warm up faster than the MI CCD. During *Opportunity*'s extended missions, mosaics of MI focal section stacks [Herkenhoff *et al.*, 2003] were often acquired, with pauses between stacks to allow the image buffer to clear. The PCB-CCD temperature difference during these pauses may increase or decrease (Fig. 4). The evolution of this temperature difference is similar during the acquisition of the first stack of images but is highly variable during subsequent stacks (Fig. 4). Complete analysis of these temperature differences is beyond the scope of this project, so we have not modeled the CCD temperature using simultaneous PCB temperature data in cases when the CCD temperature is suspect. Rather, we simply replace CCD temperature data that exceed 21°C with 0°C and add two keywords to the image label of *Opportunity* MI calibrated RDRs:

```
NOTE = "The CCD temperature greater than 21 degrees Celsius is
erroneous, so replaced with 0 degree Celsius for calibration
processing."
CCDTEMPERR = "YES"
```

While other temperature data less than 21°C returned after Sol 2611 may also be erroneous, they have not been corrected in the MI calibration pipeline processing.

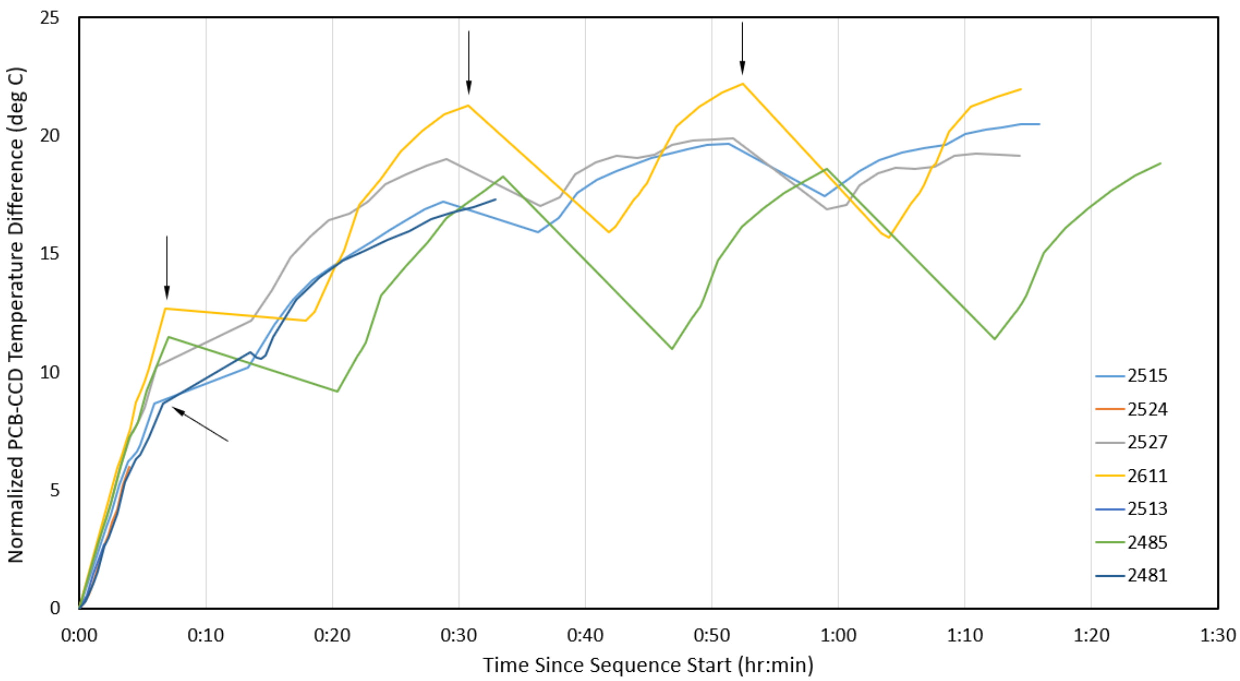

Figure 4. Normalized difference between MI PCB and CCD temperatures (°C) plotted as a function of time since start of imaging sequence for several series of MI images acquired before the CCD temperature sensor failure. Examples of beginning of pauses between stacks of MI images indicated by arrows. The sol number on which each series was acquired is shown in the legend.

The worst-case radiometric calibration error introduced by erroneous CCD temperature data is 10% (for an image taken when the CCD temperature was 21°C with a 1-second exposure time). CCD temperatures and exposure times were typically lower, so that the previously-estimated absolute radiometric calibration uncertainty of 20% [Herkenhoff *et al*., 2008] is likely valid. Every *Opportunity* MI image of the Martian surface was corrected for transfer smear using the onboard "shutter" correction capability, which corrects for variations in zero-exposure dark current [Herkenhoff *et al*., 2004]. Therefore, erroneous CCD temperatures do not increase the relative (pixel-to-pixel) radiometric calibration uncertainty of 1.5% reported by Herkenhoff *et al*. [2008]. However, quantitative analyses of MI RDRs that include the `CCDTEMPERR` keyword should recognize the possibility that the uncertainty in absolute radiometric calibration may be as high as 30% for these products.

Flat Field Response

A common technique for measuring variations in camera/telescope response across their field of view (FOV) is to acquire images of the sky above terrestrial observatories, assuming that the sky brightness is uniform across the FOV. Similarly, camera systems on Mars can be calibrated for "flat field" response by imaging the Martian sky, and MI "sky flats" were therefore periodically acquired during the *Opportunity* mission. However, this method is complicated for wide-angle cameras such as the MI because the assumption that the Martian sky brightness is uniform across the FOV is typically not valid. Because processing of MI images of the sky acquired early in the mission to correct for variations in sky brightness using simultaneous Navcam sky images [Herkenhoff *et al*., 2008] did not appear to completely remove the gradient in sky brightness, a new technique for acquiring MI sky flats was used later in the mission. As before, the MI was pointed away from the sun to avoid direct illumination of the MI optics, and nearly-simultaneous Navcam images were acquired of the same patch of sky. The new approach included a pair of MI images, separated by a 180-degree rotation of the camera about its boresight. These images were corrected for dark current and averaged to remove the sky brightness gradient. While this technique does not account for nonlinear variations in sky brightness, modeling of sky radiance indicates that such deviations from a simple gradient in sky brightness are minimal in the direction that the MI sky flats were taken (~40° above the horizon, azimuth opposite the sun; M. Lemmon, personal communication, 2004). The Navcam sky images are consistent with this model prediction and typically show no evidence for clouds in the FOV, but dust on the Navcam optical window lends some uncertainty to these conclusions. Pairs of *Opportunity* MI images of the sky were acquired using this approach starting on Sol 1899, but not all pairs were useful for calibration due to timing errors and other issues. The sky flat pairs that were most useful for calibration were taken on Sols 2086, 2181, 2416, 2585, 3053, 3126, 3321, 3427, 3700, 4066, 4340, and 4408.

MI images taken after the 2007 dust storm showed evidence for contamination of the optics (Fig. 5) even though the dust cover was closed during the storm. By design, the MI dust cover includes a labyrinth to allow gas to escape from between the dust cover and the optical window during launch, but it was not expected to allow Martian dust into the space between the dust cover and the optics. Apparently, strong storm winds carried dust through the labyrinth onto the optical window. Because changes in flat field response before the 2007 dust storm are relatively minor [Herkenhoff *et al*., 2008] and all the useful sky flat pairs listed above were acquired after the dust storm, analysis of MI sky flats focused on post-storm data and flat fields acquired before flight were used to calibrate pre-storm images.

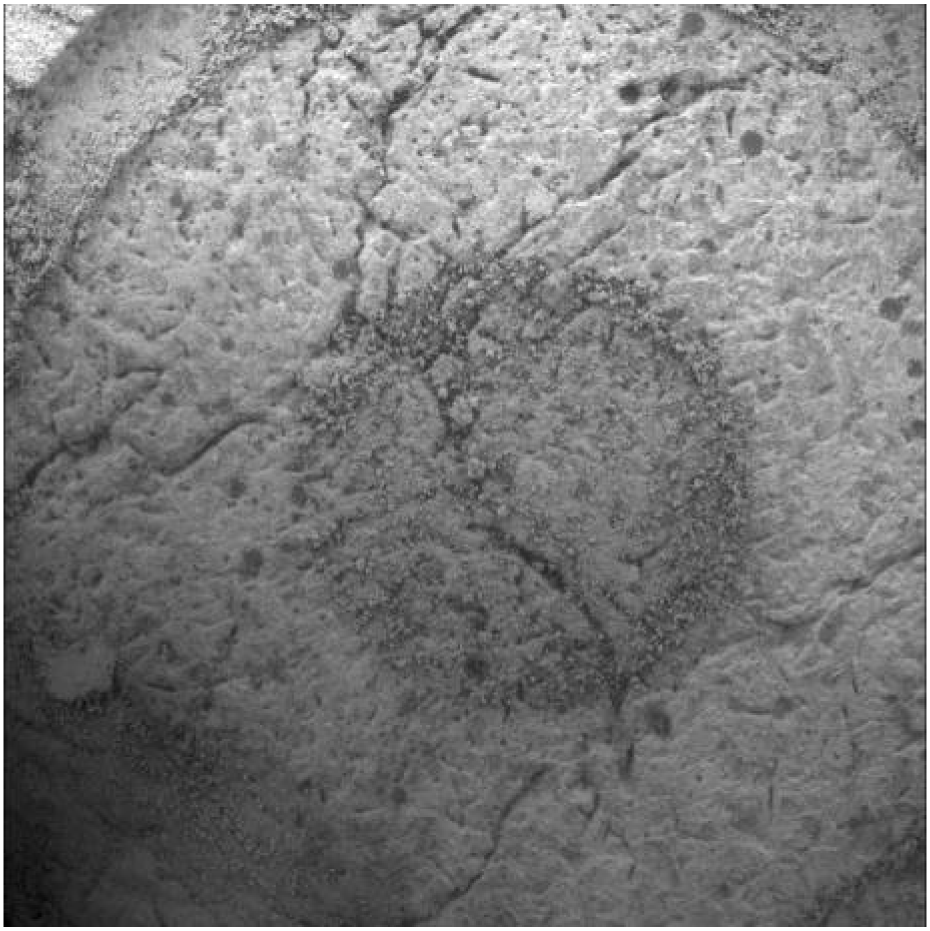

Figure 5. *Opportunity* MI image 1M245369672 of Rock Abrasion Tool target "Steno" acquired on Sol 1320 when target was fully shadowed. Lower response in lower left corner was not observed before the 2007 dust storm and was likely caused by dust contamination of the MI optics.

The best sky image pairs were normalized to the average of the central 100x100 pixels and each pair averaged. The resulting normalized sky flats show minor changes between Sols 1918 and 2416, then the Sol 2585 sky flat shows significant (~10%) change in the upper right corner. Further changes occurred by Sol 3053, and somewhat smaller changes by Sol 3321. The Sol 1918, 2086 and 2181 sky flats were used to calculate the average and standard deviation of the set. The standard deviation exceeded 0.01 at a few dozen locations due to an unusual pixel value in one of the normalized images. These atypical values were likely caused by radiation effects and were replaced with the average of the values at the same location in the other two images. Because the Sol 1918 sky flats were taken when the sun illuminated the MI optics (scattering angle less than 75 degrees), they were not included in the creation of the average sky flat that was used to correct images acquired between Sols 1250 and 2300—only the corrected Sol 2086 and Sol 2181 sky flats were averaged.

The averaged sky flats were used to correct several poorly-focused MI images. These test results were compared with images processed in the same way except using the pre-flight flat field. Statistics were extracted from areas with relatively constant pixel values and showed that the standard deviation of pixel values around the average of the area was reduced. For example, the scatter (standard deviation) of a relatively uniform part of a Sol 1287 MI image of the sky (Fig. 6) was reduced by almost 60% when corrected using the average of sky flats acquired on Sols 2086 and 2181. Individual pixel values were changed by up to 25% by the new flat field correction relative to the image processed using the pre-flight flat field, indicating a significant improvement in radiometric calibration accuracy.

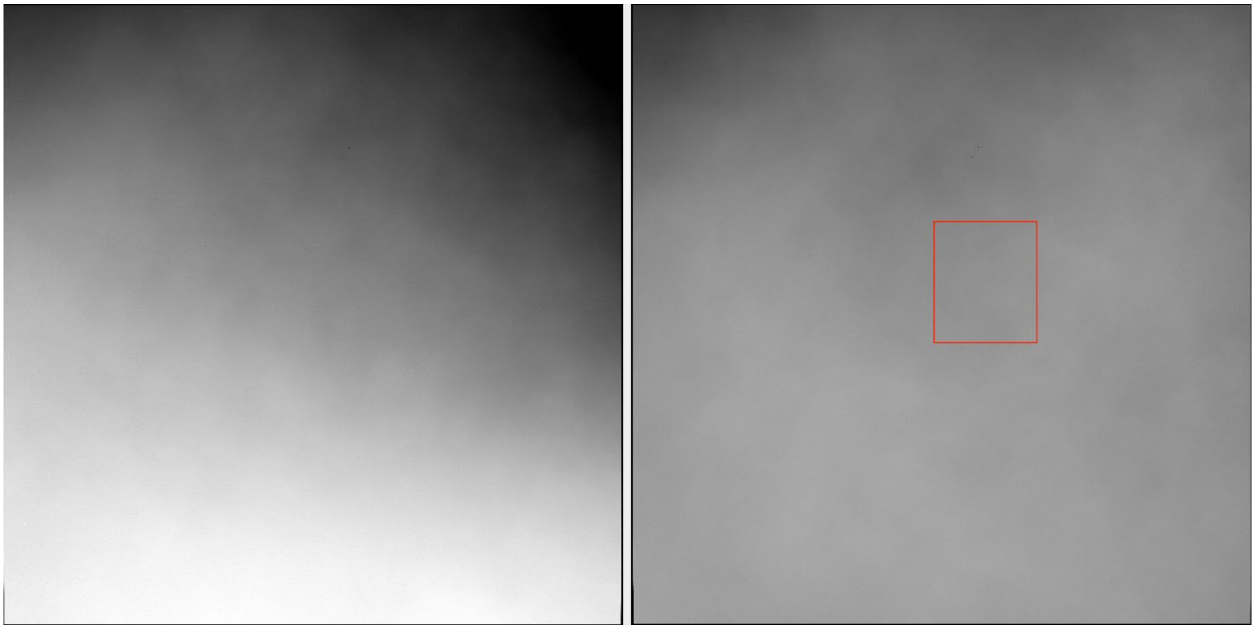

Figure 6. Sol 1287 sky image 1M242435571, taken with dust cover open before local noon when sunlight directly illuminated MI optics. Contrast enhanced so that black corresponds to *I/F* = 0.06 and white corresponds to *I/F* = 0.1. (left) Image calibrated using pre-flight flat field. (right) Image calibrated using average of sky flat acquired on Sols 2068 and 2181. Red box outlines uniform area where statistics were extracted from both images.

Significant changes in flat field response were observed before the Sol 2416 and before/after the Sol 2585 sky flats were acquired, so the averages of the images acquired on these sols were not combined. Sky flats acquired on Sols 3053 and 3126 were averaged together, as were sky flats acquired on Sols 3321, 3427, and 3700. These averaged and individual sky images were used to correct MI images taken in the sol ranges listed in Table 1. A sky image that was pointed too close to the Sun on Sol 2845 was processed using the average of the Sol 3053 and 3126 sky flats. Differences of up to 19% in pixel values between the Sol 2845 image processed using the pre-flight vs. averaged sky flats were measured, comparable to the result of the Sol 1287 image processing test. Similar tests of a poorly-focused Sol 3475 image and a Sol 4503 sky flat that was pointed too close to the horizon showed differences of up to 16% between pre-flight and averaged sky flat corrections. Image statistics extracted from uniform areas of these images also show significant reductions in the standard deviation of the pixel values in the images calibrated using averaged sky flats, indicating that the flat fields generated using sky images more accurately correct variations in camera response. Unfortunately, a packet is missing from one of the Sol 4733 sky flats, and one of the Sol 4748 sky flats is very noisy, so these data cannot be used to calibrate MI images taken late in the Opportunity mission. Rather, sky flats acquired on Sols 4066, 4340, and 4408 were averaged and used to correct all images taken after Sol 3900. The available sky flats show evidence for changes in dust contamination after Sol 4408, but they are relatively minor.

Table 1. Flat field correction ranges

Sol Range	Flat Field
1-1250	Pre-flight: 110_flatfield_tsc.cub
1251-2300	110_flatfield_2_skyflat_norm_avg.cub
2301-2500	110_flatfield_2416B_avg.cub
2501-2800	110_flatfield_2585B_avg.cub
2801-3200	110_flatfield_3000s1B_avg.cub
3201-3900	110_flatfield_3000s2B_avg.cub
3901-EOM	110_flatfield_4000sB_avg.cub

The dates of changes in flat field response due to deposition or redistribution of dust on the MI optics are not precisely known, so the selection of the sol range boundaries in Table 1 was loosely defined. This causes significant uncertainties in flat field correction accuracy: Differences between averaged post-storm sky flats and averaged pre-flight flats are as large as 25%, with a standard deviation of 9% or less. For comparison, sky flats taken before the 2007 dust storm on Sols 90, 367, and 697, corrected for the gradient in sky brightness using simultaneously-acquired Navcam images [Herkenhoff *et al.,* 2008] show differences of up to 4% relative to the pre-flight flat field (excluding radiation hits) with a standard deviation of less than 1%. Therefore, the uncertainty in absolute radiometric calibration accuracy for *Opportunity* MI images acquired before the 2007 dust storm is about 20% [Herkenhoff *et al*., 2008] and the relative radiometric calibration uncertainty is about 5%. These uncertainties are larger for images taken after the dust storm, especially during periods between sky observations: ~30% absolute and ~10% relative.

References

Herkenhoff, K. E., S. W. Squyres, J. F. Bell III, J. N. Maki, H. M. Arneson, P. Bertelsen, D. I. Brown, S. A. ColLins, A. Dingizian, S. T. Elliott, W. Goetz, E. C. Hagerott, A. G. Hayes, M. J. Johnson, R. L. Kirk, S. McLennan, R. V. Morris, L. M. Scherr, M. A. Schwochert, L. R. Shiraishi, G. H. Smith, L. A. Soderblom, J. N. Sohl-Dickstein, and M. V. Wadsworth (2003). Athena Microscopic Imager Investigation. *J. Geophys. Res*. **108**, 8065, doi:10.1029/2003JE002076.

Herkenhoff, K., R. Kirk, M. Rosiek, L. Soderblom, B. Sucharski, J. Torson, J. Bell, H. Arneson, A. Hayes, M. Johnson, J. Sohl-Dickstein, D. Brown, A. Collins, A. Dingizian, T. Elliot, J. Maki, L. Scherr, M. Schwochert, D. Thiessen, and M. White (2004). Mars Exploration Project Microscopic Imager Calibration Report, Rev. B. JPL D-19830, MER 420-6-704.

Herkenhoff, K. E., J. P. Grotzinger, A. H. Knoll, S. M. McLennan, C. M. Weitz, R. A. Yingst, R. C. Anderson, B. Archinal, R. E. D. Arvidson, J. Barrett, K. J. Becker, J. F. Bell, C. Budney, M. G. Chapman, D. A. Cook, B. L. Ehlmann, B. J. Franklin, L. R. Gaddis, D. Galuszka, P. Garcia, P. E. Geissler, T. M. Hare, E. Howington-Kraus, J. R. Johnson, L. Keszthelyi, R. L. Kirk, P. D. Lanagan, E. M. Lee, C. Leff, J.

Maki, K. F. Mullins, T. Parker, B. Redding, M. Rosiek, M. H. Sims, L. A. Soderblom, N. Spanovich, R. Springer, S. W. Squyres, D. Stolper, R. Sucharski, T. Sucharski, R. J. Sullivan, and J. Torson (2008), Surface processes recorded by rocks and soils on Meridiani Planum, Mars: Microscopic Imager observations during Opportunity's first three extended missions, *J. Geophys. Res*. **113**, E12S32, doi:10.1029/2008JE003100.